Research article

Hao Yang, He Liu, Boxiang Song, Yuanrui Li, Deming Meng, Buyun Chen, Pan Hu, Yunxiang Wang, Tse-Hsien Ou, Michelle L. Povinelli and Wei Wu*

Effects of roughness and resonant-mode engineering in all-dielectric metasurfaces

https://doi.org/10.1515/nanoph-2019-0501
Received December 3, 2019; revised February 13, 2020; accepted March 7, 2020

Abstract: The development of all-dielectric metasurfaces vigorously prompts the applications of optical metasurfaces for the visible and near-IR light range. Compared to IR or longer wavelength light, visible and near-IR light have shorter wavelengths. As a result, surface roughness and imperfections of all-dielectric metasurfaces have larger scattering or absorption of visible and near-IR light, thereby directly affecting the performance of an all-dielectric metasurface. In this article, a volume-current method is adopted to study the effect of metasurface roughness. Numerical calculations based on the finite difference time domain (FDTD) method are also used to study the relationship between the effects of metasurface roughness and the optical resonant modes. Numerical predictions based on our theoretical studies fit the experimental data well. Further, the effect of different roughness levels on the all-dielectric metasurface performance is predicted. More importantly, a method utilizing resonant-mode engineering to enhance the metasurface performance (e.g. incident angle insensitivity) is also proposed and demonstrated. This work deepens our understanding of the working mechanism of all-dielectric metasurfaces and paves the way for their use in a broad spectrum of applications.

Keywords: all-dielectric metasurface; high-contrast grating; roughness; hybrid metasurface; resonant-mode engineering.

***Corresponding author: Wei Wu,** Ming Hsieh Department of Electrical and Computer Engineering, University of Southern California, Los Angeles, CA 90089, USA, e-mail: wu.w@usc.edu. https://orcid.org/0000-0001-6404-0317
Hao Yang, He Liu, Boxiang Song, Yuanrui Li, Deming Meng, Buyun Chen, Pan Hu, Yunxiang Wang, Tse-Hsien Ou and Michelle L. Povinelli: Ming Hsieh Department of Electrical and Computer Engineering, University of Southern California, Los Angeles, CA 90089, USA

1 Introduction

The nature of all-dielectric metasurfaces ensures their high transmission and diffraction efficiencies compared to plasmonic nanostructures [1–7]. In recent years, the development of all-dielectric metasurfaces has vigorously promoted the applications of optical metasurfaces for the visible and near-IR light; examples include flat lenses [8], spectrum splitters [9–11], ultra-broadband reflectors [12], and full-color reflective displays [13–15]. Unfortunately, due to the imperfections in the fabrication process, roughness of all-dielectric metasurfaces is inevitable. With the wavelength of the manipulated light decreasing from the IR range to the visible and near-IR range, the metasurface roughness has a larger effect on its performance. Previous works have dealt with the effects of fabrication errors (e.g. dimensional deviations and steepness angle of nanopillars) on the performance of metasurfaces [16, 17]. However, it is still unclear how random metasurface roughness affects the metasurface's performance. Also, the performance of the all-dielectric metasurface still needs to be enhanced in order for it to be used in some applications in the visible light range (e.g. full-color reflective display).

In this article, with the red light (625–740 nm) band reflector of a full-color display system based on all-dielectric metasurfaces as an example, the effects of metasurface roughness on its performance are analyzed. According to the volume-current method [18], the all-dielectric metasurface roughness can be considered equivalent to a lossy shell. Further, numerical calculations utilizing the finite difference time domain (FDTD) method are performed to study the optical resonant modes of the all-dielectric metasurface. The results reveal the relationship between the distributions of resonant modes and the effects of metasurface roughness. Besides, analyses of the metasurface performance depending on the roughness level are performed, which provides a guidance in designing metasurfaces for better manufacturability. More importantly, a method to enhance the metasurface's performance through engineering the resonant modes is

Open Access. © 2020 Wei Wu et al., published by De Gruyter. This work is licensed under the Creative Commons Attribution 4.0 Public License.

proposed. The feasibility of this method is demonstrated by an example using a hybrid metasurface structure to improve the incident angle insensitivity of the red light band reflector.

2 Results and discussion

2.1 Roughness and imperfection of fabricated metasurfaces

There are many applications of all-dielectric metasurfaces. One example is a full-color reflective display system based on such metasurfaces [13–15], which provides a promising solution to problems with current mobile device screens, such as high energy consumption and lack of readability under bright sunlight. The full-color reflective display system contains three tandem band reflectors (blue, green, and red), all of which are constructed by all-dielectric metasurfaces. However, due to imperfections in fabrication, there are differences between the designed metasurfaces (ideal metasurfaces) and the fabricated ones.

Figure 1A–C shows the schematic of an ideal all-dielectric metasurface, the schematic of the fabricated all-dielectric metasurface, and the SEM images of the fabricated three-color (blue, green and red) band reflector based on the all-dielectric metasurface, respectively. These images clearly indicate that the fabricated all-dielectric metasurfaces are different from the ideal one. As shown in Figure 1A, each nanopillar of the ideal all-dielectric metasurface is a frustum with smooth surfaces. However, the nanopillars in the fabricated all-dielectric metasurfaces (Figure 1B and C) are imperfect. There are

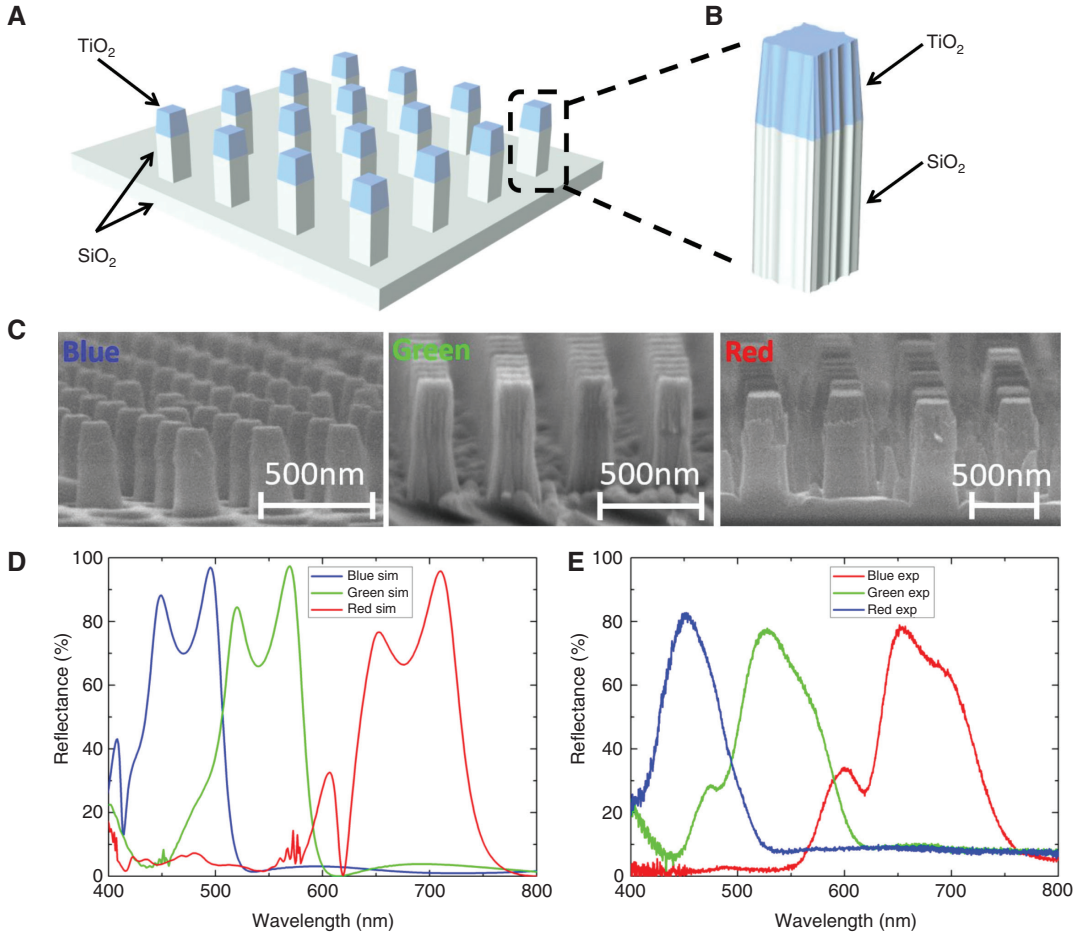

Figure 1: All-dielectric metasurfaces for visible light range applications.
(A) Schematic of the ideal all-dielectric metasurface. The nanopillar is a frustum with smooth surfaces. (B) Schematic of the fabricated all-dielectric metasurface. The surfaces of nanopillar are rough. (C) SEM images of fabricated band reflector based on all-dielectric metasurfaces for blue, green, and red light, respectively. (D) Calculated reflection spectra of the ideal all-dielectric metasurfaces (A). (E) Measured reflection spectra of the fabricated all-dielectric metasurfaces (C), which are obviously different from the calculated spectra.

some "bumps" on the nanopillar surface, which makes the surface rough.

For band reflectors used in the visible light range, the wavelength of the manipulated light is in the range 380–740 nm [19], which is much shorter than that of IR light. As a result, the roughness or imperfection of the all-dielectric metasurface has a large effect on its performance. For each band reflector, there are two reflection peaks in the calculated reflection spectrum (Figure 1D) when the ideal metasurface structure (Figure 1A) is used for numerical calculations. However, only one peak is observed in the measured reflection spectrum (Figure 1E). These data were obtained from the fabricated band reflector (Figure 1C). It is especially noticeable that all three band reflectors lose the reflection peak at longer wavelengths. This indicates that the effects of metasurface roughness are not even. Since the two reflection peaks represent different optical resonant modes, the metasurface roughness should have different effects on different optical resonant modes.

2.2 Effects and study of the metasurface roughness

To study how the roughness of the metasurface affects its performance, the red light band reflector based on an all-dielectric metasurface is taken as an example. Figure 2A and B shows the schematic of the all-dielectric metasurface for the red light band reflector and the corresponding calculated reflection spectrum at normal incidence, respectively. The incident light is unpolarized in Figure 2B. The all-dielectric metasurface contains a nanopillar array on a SiO_2 substrate, and each nanopillar has two layers (TiO_2 and SiO_2). There are two reflection peaks in the calculated spectrum at 652 and 710 nm. As mentioned above, the peak at the longer wavelength (710 nm) is absent in the measured spectrum (Figure 1E).

Figure 2C shows the $|\boldsymbol{E}|^2$ distributions of the ideal all-dielectric metasurface at different wavelengths (652 or 710 nm) in different planes (*YZ*- or *XZ*-plane). Both the *YZ*- and *XZ*-planes go through the nanopillar center. Because of the symmetry of our all-dielectric metasurface, the reflection spectrum is independent of the polarization at normal incidence [15]. To show the resonant modes clearly, the incident light is set to propagate along the *z*-axis and is *y*-polarized in Figure 2C and D. It is obvious that the electrical field in the *YZ*-plane is much larger than that in the *XZ*-plane; therefore, the field distribution in the *YZ*-plane is a better representation of the optical resonant modes. Therefore, the following discussion will be focused on the *YZ*-plane. Although the TiO_2 layer of the nanopillar is a frustum, the nanopillar sidewalls are almost perpendicular to the *y*-axis in the *YZ*-plane. Hence, $E_{\parallel}=\sqrt{E_x^2+E_z^2}$ and $\boldsymbol{E}_{\perp}=\boldsymbol{E}_y$ are used here to represent the electrical field components that are parallel or perpendicular to the nanopillar surface, approximately. Figure 2D shows the distribution of the electrical field components ($\boldsymbol{E}_{\parallel}$ or $\boldsymbol{E}_{\perp}$) at 652 or 710 nm in the *YZ*-plane. Comparing the four field distributions in Figure 2D, it can be observed that $\boldsymbol{E}_{\parallel}$ and $\boldsymbol{E}_{\perp}$ contribute almost equally to the optical resonance at 652 nm, while $\boldsymbol{E}_{\parallel}$ contributes much more to the optical resonance at 710 nm than $\boldsymbol{E}_{\perp}$. In addition, at both wavelengths (652 and 710 nm), $\boldsymbol{E}_{\parallel}$ overlaps with the nanopillar sidewalls significantly, while $\boldsymbol{E}_{\perp}$ is mainly distributed inside the nanopillar.

The metasurface roughness can be regarded as "bumps" on the metasurface sidewalls. Intuitively, these "bumps" should have different effects on $\boldsymbol{E}_{\parallel}$ and $\boldsymbol{E}_{\perp}$ because the distributions of $\boldsymbol{E}_{\parallel}$ and $\boldsymbol{E}_{\perp}$ are different. In addition, $\boldsymbol{E}_{\parallel}$ is oscillating along these "bumps", so $\boldsymbol{E}_{\parallel}$ receives larger scattering or absorption from these "bumps" compared to $\boldsymbol{E}_{\perp}$. Also, Figure 2C and D shows that the electrical fields are mainly distributed in the TiO_2 layer. The refractive index of TiO_2 (around 2.6) is much higher than that of SiO_2 (around 1.5) [12, 14, 20]. As a result, the roughness of the TiO_2 layer has a larger effect on the metasurface's performance. In the following discussion, only the roughness of the TiO_2 layer will be considered. Moreover, the nanopillar shape is adjusted to frustum in order to fit the real situations better.

As mentioned above, the FDTD method is adopted to carry out numerical calculations in this work. In these calculations, a periodic boundary condition is applied. If structural imperfection is added directly to the unit cell to simulate the roughness, this roughness becomes a part of the unit cell and hence periodic. The periodic features and random features scatter light very differently, so we cannot directly put the roughness feature into the unit cell to study the effects of surface roughness. Hence, a thin lossy layer is added to the nanopillar surface to mimic the surface roughness equivalently. Here, the volume-current method is adopted [18]. TiO_2 and the background ($n=1$) have high refractive index contrast, so the TiO_2 bump is in a high-index-contrast boundary with a small volume ΔV and a shift in the dielectric constant Δe. The electric field will induce a dipole moment in the bump by inducing charge density $\Delta\rho$, as shown in Figure 3A. This induced dipole moment can be expressed as

$$p=\Delta V(\alpha_{\parallel}E_{\parallel}+\gamma_{\perp}D_{\perp}) \tag{1}$$

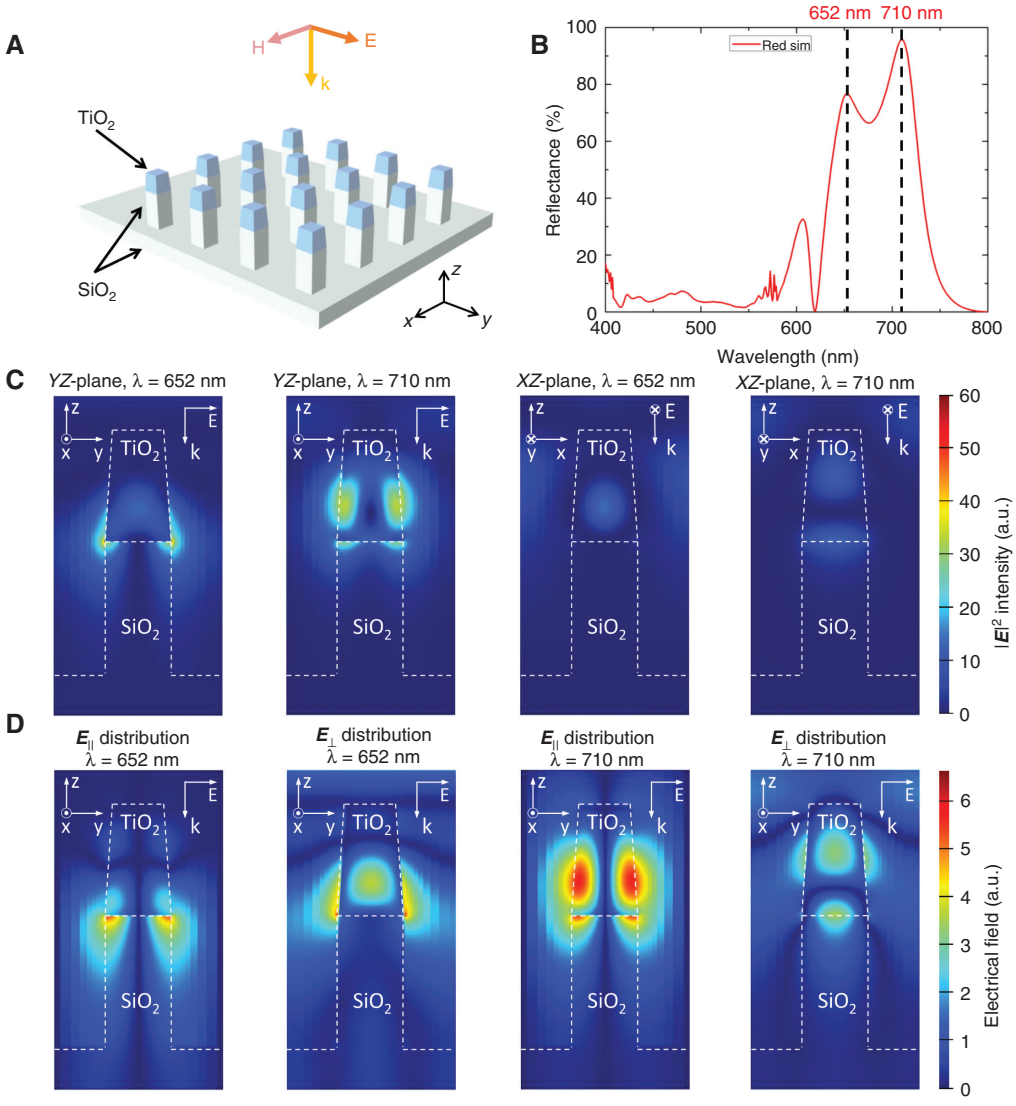

Figure 2: Numerical calculations of the ideal all-dielectric metasurface.
(A) Schematic of the ideal all-dielectric metasurface for the red light band reflector, which has two layers (TiO_2 and SiO_2). (B) Calculated reflection spectrum of the ideal all-dielectric metasurface at normal incidence. There are two reflection peaks at 652 and 710 nm. (C) $|\boldsymbol{E}|^2$ distributions of the ideal all-dielectric metasurface at different wavelengths (652 or 710 nm) in different planes (*YZ*-plane or *XZ*-plane). (D) Electrical field component ($\boldsymbol{E}_\parallel$ or $\boldsymbol{E}_\perp$) distributions of the ideal all-dielectric metasurface at different wavelengths (652 or 710 nm) in the *YZ*-plane, where $\boldsymbol{E}_\parallel = \sqrt{\boldsymbol{E}_x^2 + \boldsymbol{E}_z^2}$ and $\boldsymbol{E}_\perp = \boldsymbol{E}_y$. $\boldsymbol{E}_\parallel$ represents the electrical field component that is parallel to the nanopillar surface, while $\boldsymbol{E}_\perp$ represents the electrical field component that is perpendicular to the nanopillar surface.

where $\alpha_\parallel$ and $\gamma_\perp$ are polarizability tensors, and $\boldsymbol{E}_\parallel$ and $\boldsymbol{D}_\perp$ are the surface parallel and perpendicular components. Polarizability tensors $\alpha_\parallel$ and $\gamma_\perp$ are determined by the shape of the bump.

The oscillation of the induced dipole will cause energy loss [21]. The total time-averaged power radiated by a harmonically oscillating electric dipole is

$$P = \frac{\mu_0 \omega^4 p^2}{12\pi c} \tag{2}$$

where ω is the angular frequency, p is the dipole moment, μ_0 is the permeability in the vacuum, and c is the light speed in vacuum.

Since the material is linear and isotropic, $\boldsymbol{D}_\perp = \varepsilon \boldsymbol{E}_\perp$, where ε is the material permittivity. $\alpha_\parallel$ and $\gamma_\perp$ are diagonal. Substituting Eq. (1) into Eq. (2), we get

$$P = \frac{\mu_0 \omega^4 \Delta V^2 (\alpha_\parallel \alpha_\parallel E_\parallel^2 + \gamma_\perp \gamma_\perp D_\perp^2)}{12\pi c}$$
$$= \frac{\mu_0 \omega^4 \Delta V^2}{12\pi c} (\alpha_\parallel \alpha_\parallel E_\parallel^2 + \gamma_\perp \gamma_\perp \varepsilon^2 E_\perp^2) \tag{3}$$

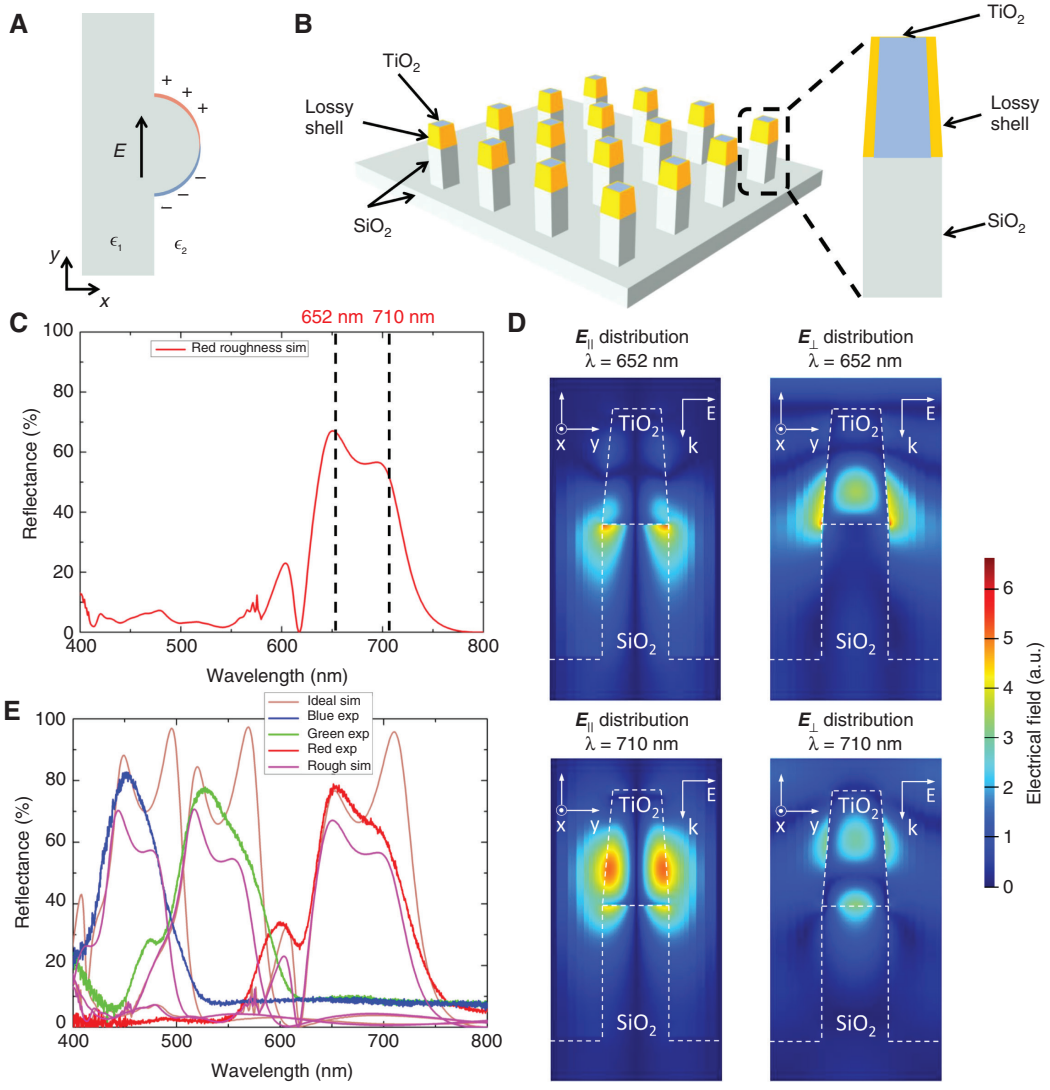

Figure 3: Effects of metasurface roughness.
(A) A "bump" on the interface between two materials e_1 (TiO_2) and e_2 (background). An applied electric field E will induce a dipole moment on the surface (blue/red color denotes positive/negative charge). (B) Schematic of all-dielectric metasurface with a lossy shell. The 5-nm-thick lossy shell is outside the TiO_2 layer. (C) Calculated reflection spectrum of the all-dielectric metasurface with the lossy shell (B) at normal incidence. (D) Electrical field component ($\boldsymbol{E}_{\parallel}$ or $\boldsymbol{E}_{\perp}$) distributions of the all-dielectric metasurface with the lossy shell (B) at different wavelengths (652 or 710 nm) in the *YZ*-plane. (E) Calculated reflection spectra of the ideal all-dielectric metasurfaces (Figure 1A), measured reflection spectra of the fabricated all-dielectric metasurfaces (Figure 1B and C), and calculated reflection spectra of the all-dielectric metasurface with the lossy shell (B). All spectra are at normal incidence. It is obvious that the calculated reflection spectra of the all-dielectric metasurface with the lossy shell are much closer to the measured spectra.

Equation (3) shows that the parallel and perpendicular components of the electrical field ($\boldsymbol{E}_{\parallel}$ and $\boldsymbol{E}_{\perp}$) are scattered differently by the bumps (roughness); therefore they have different contributions to the energy loss. In other words, the bumps have different effects on the parallel and perpendicular components ($\boldsymbol{E}_{\parallel}$ and $\boldsymbol{E}_{\perp}$). Considering that the radiation loss due to the roughness and the material loss on the surface have the same effect on the optical resonant modes [22], the metasurface roughness effect can be considered equivalent to a lossy shell added to the nanopillar (Figure 3B). The index of the lossy shell is $n_{\text{lossy shell}} = n + ik$, where n is the refractive index of TiO_2, and k is the absorption constant. Since roughness has different effects on the parallel and perpendicular components, $k = \begin{pmatrix} k_{xx} & 0 & 0 \\ 0 & k_{yy} & 0 \\ 0 & 0 & k_{zz} \end{pmatrix}$. By adjusting the values of k_{xx}, k_{yy}, and k_{zz}, the effect of roughness on the nanopillar sidewalls can be simulated equivalently.

Figure 3C shows the calculated reflection spectrum of the all-dielectric metasurface with the lossy shell (Figure 3B) at normal incidence. It is noticeable that the peak at longer wavelength (710 nm) receives much larger effects from the lossy shell, which fits the experimental results quite well. Figure 3D shows the distributions of the electrical field component ($\boldsymbol{E}_{\parallel}$ or $\boldsymbol{E}_{\perp}$) of the all-dielectric metasurface with the lossy shell (Figure 3B) at different wavelengths (652 or 710 nm) in the *YZ*-plane. Notice that the color scale bar in Figure 3B is same as in Figure 2D. Compared to those in Figure 2D, the distributions of the resonant modes have barely changed. However, the resonance intensity at 710 nm has decreased considerably, which is in accord with Figure 3C.

Figure 3E shows the calculated reflection spectra of the ideal all-dielectric metasurface (Figure 1A), the measured reflection spectra of the fabricated all-dielectric metasurface, (Figure 1B and C), and the calculated reflection spectra of the all-dielectric metasurface with the lossy shell (Figure 3B). These spectra indicate that the numerical calculations with the lossy shell fit the experimental results much better, which demonstrates the validity of our assumption and derivation.

From the above discussion, it is clear that our proposed volume-current method has established a way to simulate the effects of random roughness equivalently. By comparing the experimental spectra and numerically calculated spectra, the equivalent loss (i.e., k_{xx}, k_{yy}, and k_{zz}) of the lossy shell corresponding to the as-fabricated roughness level can be extracted. Based on those, the effects of different levels of roughness on the metasurface performance can be predicted. Assuming that the average roughness scale is ΔL, the bump volume is proportional to ΔL^3. Figure 1C shows that the nanopillar sidewall is fully occupied by "bumps" (roughness). In this case, in unit area of the nanopillar surface, the total "bump" volume should be proportional to ΔL. Using Eq. (3), the radiated power should be proportional to ΔL^2: in other words

$$P \propto \Delta L^2 \tag{4}$$

The metasurface roughness is mainly determined by fabrication techniques. Our fabricated all-dielectric metasurfaces (Figure 1C) all have the same level of roughness. Using the fabricated red band reflector as an example, Figure 4A and B shows the top-view SEM image of the fabricated all-dielectric metasurface and the corresponding edge detection result (more images can be found in Supporting Information Figure S1). From the edge detection result, the average roughness (3σ) scale can be calculated, which is 8 nm. Using our proposed lossy shell method and Eq. (4), the effects of different level roughness on metasurface's performance are calculated numerically (Figure 4C).

Through fitting the reflection spectrum, the effects of different levels of roughness on different resonant modes can be revealed. Figure 4D shows the resonant-mode extraction using the measured spectrum of a fabricated all-dielectric metasurface as an example. Figure 4E and F shows the resonant-mode extraction results for Figure 4C and the change in value of two peaks in the reflection spectra with respect to the change in the roughness level, respectively. More separated resonant-mode extraction results can be found in Supporting Information (Figures S2–S9). It is obvious that a higher level roughness has much more effect on the resonant mode at the second main optical resonance, which is consistent with the above results (Figures 2C, D, and 3D). These analyses explain the effect of different roughness levels on the performance of all-dielectric metasurfaces, which could provide a guidance in designing more practical metasurfaces by taking into consideration the nanofabrication capability.

2.3 Engineering of resonant modes

Our experimental and theoretical data indicate that surface roughness has different effects on different resonant modes according to the field distribution of each resonant mode. This causes the absence of the peak at longer wavelengths in all three spectra of Figure 1E. Inspired by this, we propose a method to engineer the resonant modes by adding high-loss material in certain locations. Through precise design, we can keep the desired resonant modes while weakening the unwanted modes simultaneously.

Optical metasurfaces are usually sensitive to the incident angle [23–25], which limits their applications. For example, the incident angle sensitivity limits the viewing angle of a reflective display system based on all-dielectric metasurfaces [15]. Using the red light band reflector as the example, Figure 5A and B shows the schematics of the all-dielectric metasurface at oblique incidence and the calculated reflection spectra of the all-dielectric metasurface versus the incident angle, respectively. As shown in Figure 5B, the reflection spectra of the red band reflector change significantly with the change in the incident angle. Since the incident light for the red light band reflector in a real situation is unpolarized, the incident light was set as unpolarized in numerical calculations (Figure 5B). The wavelength for red light ranges from 625 to 740 nm

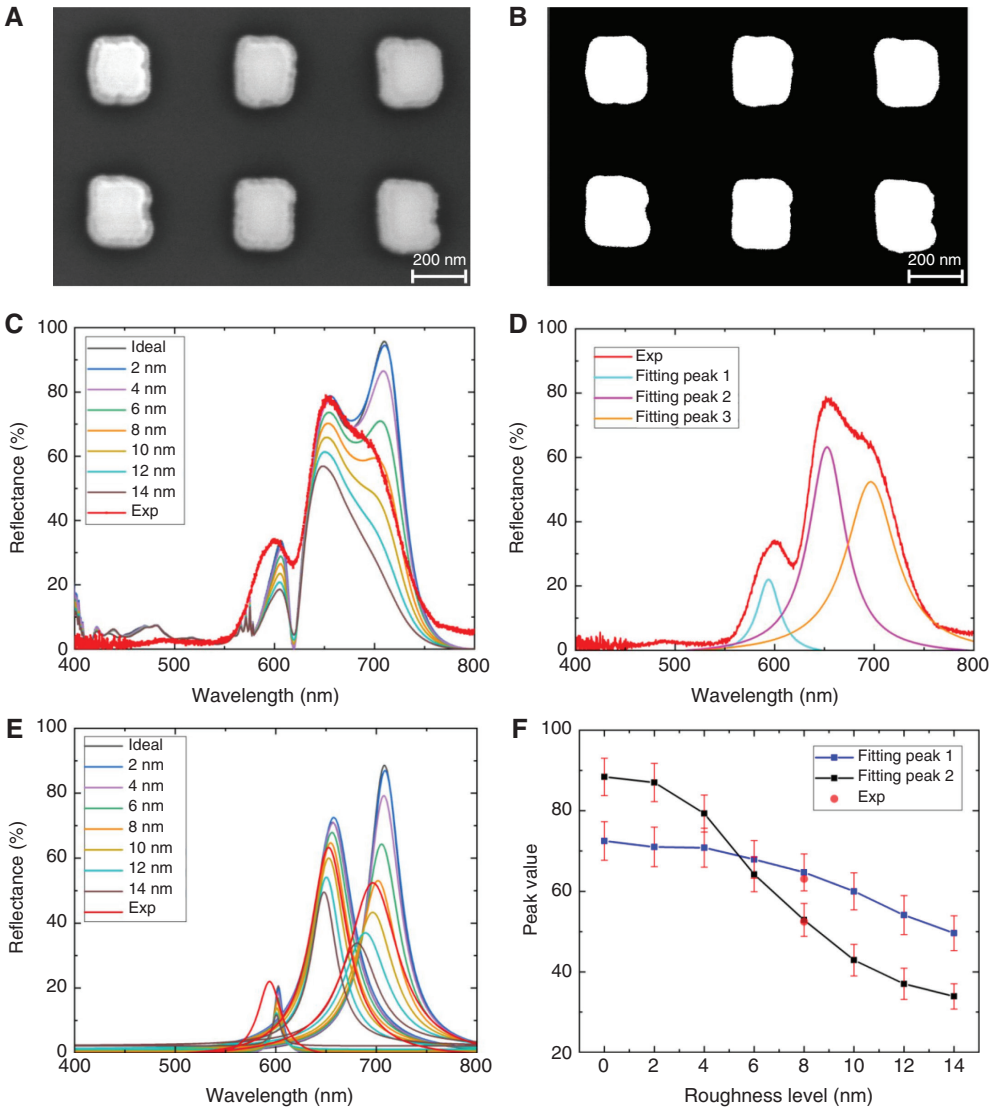

Figure 4: Calculated results of effects of different level roughness.
(A) Top-view SEM image of all-dielectric metasurface. The roughness of nanopillars can be observed clearly. (B) Edge detection result of SEM image in (A). The average roughness scale is 8 nm (3σ). (C) Calculated reflection spectra with different levels of roughness and the measured reflection spectrum of the all-dielectric metasurface at normal incidence. (D) Resonant-mode extraction from fitting the measured reflection spectrum of fabricated all-dielectric metasurface. The three fitted peaks are at 594, 653, and 697 nm, respectively. Note that the second (653 nm) and third (697 nm) peaks correspond to the main optical resonances. The first peak (594 nm) represents the side lobe in the shorter wavelength region. (E) Resonant-mode extraction for the calculated reflection spectra in (C). Higher level of roughness has much more effect on the second peak, which is consistent with previous conclusion. (F) The change of the two fitting peaks in the reflection spectra with respect to the roughness level. The two red points are the experimental results, which demonstrate the effectiveness of the calculations.

[19], so the ideal red band reflector should reflect all the incident light in this range (625–740 nm) without reflecting any other wavelength. The red light band reflector based on all-dielectric metasurface works well at normal incidence (Figure 3E). However, its performance falls at oblique incidence (Figure 5B). This can be demonstrated by Figure 5C. The reflected light color changes from red to pink gradually with increasing incident angle from 0° to 39°. This phenomenon has two causes. First, side lobes less than 625 nm (unwanted resonant modes) appear in the reflection spectra with the increase in incident angle. Second, the reflection intensity of the light between 625 and 740 nm (desired resonant modes) decreases with the increase in the incident angle.

Previously, several methods (e.g. plasmonic systems) have been demonstrated to improve the incident angle

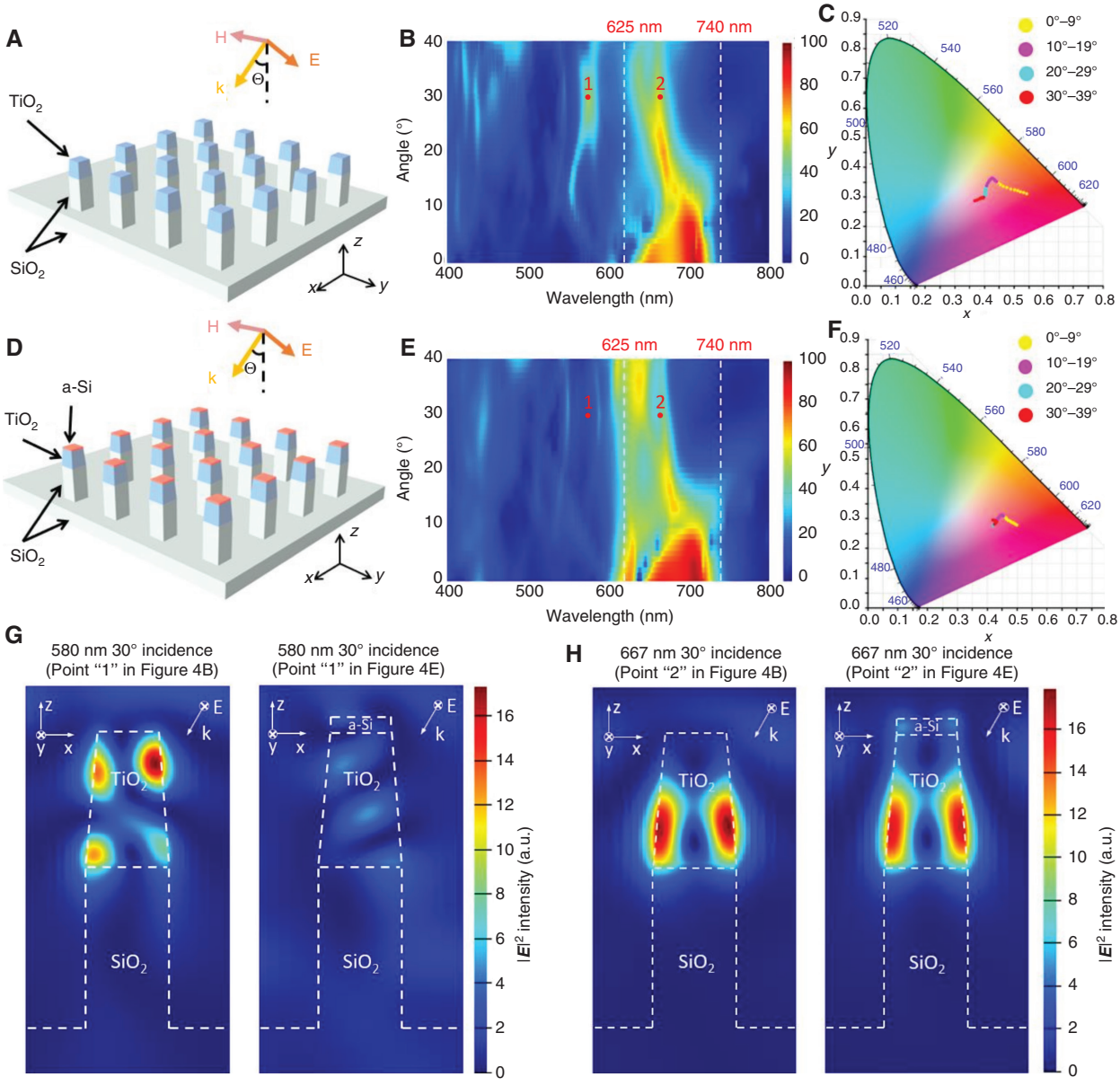

Figure 5: Resonant mode engineering.
(A) Schematic of the all-dielectric metasurface at oblique incidence. (B) Calculated reflection spectra of the all-dielectric metasurface (A) versus the incident angle. (C) The numerically calculated color of the all-dielectric metasurface (A) versus the incident angle shown in a CIE 1931 color map. (D) Schematic of the all-dielectric metasurface with an a-Si cap at oblique incidence. The thickness of the a-Si cap is 40 nm. (E) Calculated reflection spectra of the all-dielectric metasurface with an a-Si cap (D) versus the incident angle. (F) The numerically calculated color of the all-dielectric metasurface with an a-Si cap (D) versus the incident angle shown in a CIE 1931 color map. (G) $|\boldsymbol{E}|^2$ distributions of the all-dielectric metasurface with (A) and without (D) an a-Si cap upon 30° incidence at 580 nm. The left and right field distributions correspond to the point "1" in (B and E), respectively. (H) $|\boldsymbol{E}|^2$ distributions of the all-dielectric metasurface with (A)/without (D) an a-Si cap upon 30° incidence at 667 nm. The left and right field distributions correspond to the point "2" in (B and E), respectively.

insensitivity [24, 26–28]. However, these methods cannot be used to improve the performance of all-dielectric metasurfaces. Fortunately, the intensities and distributions of the desired resonant modes and unwanted modes are different, as shown in the left field distributions in Figure 5G and H, respectively. It is noteworthy that the incident light is set as *y*-polarized here in order to provide the distributions of resonant modes clearly. If the incident light is set as *x*-polarized, the results are very similar. The unwanted resonant modes are mainly distributed at

the top part of the TiO_2 layer, while the desired resonant modes are mainly distributed at lower positions. Amorphous Si (a-Si) is a high-index, high-loss material, and its absorption of short wavelength light is stronger than that of longer wavelength light. Hence, a method based on engineering the resonant modes is proposed (Figure 5D). A 40-nm a-Si cap is added to each nanopillar to construct a hybrid nanopillar. The unwanted resonant modes overlap with the a-Si cap, while desired resonant modes are located far from the a-Si cap. Also, the unwanted resonant modes have shorter wavelengths compared to the desired resonant modes. As a result, this method can weaken the unwanted resonant modes without significantly affecting the desired resonant modes. Figure 5E shows the calculated reflection spectrum of the all-dielectric metasurface with an a-Si cap versus the incident angle, and Figure 5F shows the reflected color of the all-dielectric metasurface with an a-Si cap versus the incident angle. It can be seen that the side lobes have decreased in the reflection spectra. In addition, the reflection in the red light range (625–740 nm) also has increased. This is because a-Si is also a high-index material. Although a-Si is highly lossy, its high index (around 4.0) [12] can confine the incident light effectively and enhance the optical resonance. The right field distributions in Figure 5G and H show that the intensities and distributions of the desired resonant modes and unwanted modes have huge differences after adding the a-Si cap. It is noticeable that the unwanted resonant modes almost disintegrate, while the desired resonant modes still have high intensities. Hence, the change in the reflected light color of the metasurface in Figure 5E is much smaller compared to Figure 5B. All these performance enhancements demonstrate the feasibility and validity of improving all-dielectric metasurface performance through engineering the resonant modes.

In conclusion, we proposed, demonstrated, and experimentally verified a method to analyze the effect of roughness on the performance of a metasurface. Using the volume-current method, the metasurface roughness can be considered as equivalent to a lossy shell outside the nanopillar. Based on the FDTD method, different resonant modes were also studied. We demonstrated that the different effects of the metasurface roughness on different resonant modes are due to the different resonance distributions. In other words, the all-dielectric metasurface's performance can be affected specifically by disturbing specific resonant modes. Further, the effects of different levels of roughness on metasurface's performance were predicted. This can help in designing more manufacturable all-dielectric metasurfaces based on the fabrication capability. Moreover, a method to enhance metasurface's performance based on resonant-mode engineering was proposed. A high-index, high-loss dielectric material (a-Si) can be placed in an appropriate position to weaken unwanted resonant modes without affecting the desired resonant modes. An example of improving the incident angle insensitivity of the red light band reflector demonstrated the feasibility of this method. We anticipate that, through engineering the resonant modes precisely, all-dielectric metasurfaces can be used for a broad spectrum of applications in the near future.

3 Experimental section

3.1 Numerical calculations

In this work, all the numerical analyses were performed by the FDTD method implemented with a commercial software (FDTD Solutions, Lumerical Inc.). All numerical calculations were performed under periodic or Bloch boundary conditions. In Figures 1D, 2B, 3C, 3E, 4C, 5B, 5C, 5E, and 5F, the input light source was set as collimated and unpolarized, with wavelengths ranging from 400 to 800 nm. In Figures 2C, 2D, 3D, 5G, and 5H, the input light source was set as collimated and *y*-polarized, with the wavelength ranging from 400 to 800 nm. The values of k_{xx}, k_{yy}, and k_{zz} for each band reflector in Figure 3E are determined by fitting the measured spectra with the numerically calculated spectra.

3.2 Optical characterization

The reflection spectra were measured with an Ocean Optics USB4000 spectrometer.

3.3 Fabrication

The all-dielectric metasurfaces were fabricated via nanoimprint lithography (NIL) [29–33] employing the following series of processes. TiO_2 was first deposited on a clean SiO_2 substrate by sputtering. Then, the patterns on the nanoimprint mold were transferred to the TiO_2 surface using NIL followed by reactive ion etching, metal deposition, and lift-off. Finally, TiO_2 and SiO_2 were etched by reactive ion etching to get the metasurface. The metasurface nanoimprint molds were also obtained from a series of processes. First, one-dimensional Si gratings were fabricated via interference lithography. Then, the line width of the

one-dimensional gratings were tuned to desired values by angled evaporation [34]. After that, two steps of NIL were carried out to obtain the metasurface molds with the line width-tuned one-dimensional grating mold.

Acknowledgments: The fabrications were performed at the Keck Photonics Center at the University of Southern California. The SEM images were taken at Core Center of Excellence in Nano Imaging at the University of Southern California.

References

[1] Jahani S, Jacob Z. All-dielectric metamaterials. Nat Nanotechnol 2016;11:23.
[2] Zhou Y, Huang MC, Chase C, et al. High-index-contrast grating (HCG) and its applications in optoelectronic devices. IEEE J Sel Top Quantum Electron 2009;15:1485–99.
[3] Ziolkowski RW. Propagation in and scattering from a matched metamaterial having a zero index of refraction. Phys Rev E 2004;70:046608.
[4] Smolyaninov II, Smolyaninova VN, Kildishev AV, Shalaev VM. Anisotropic metamaterials emulated by tapered waveguides: application to optical cloaking. Phys Rev Lett 2009;102:213901.
[5] Sautter J, Staude I, Decker M, et al. Active tuning of all-dielectric metasurfaces. ACS Nano 2015;9:4308–15.
[6] Shalaev MI, Sun J, Tsukernik A, Pandey A, Nikolskiy K, Litchinitser NM. High-efficiency all-dielectric metasurfaces for ultracompact beam manipulation in transmission mode. Nano Lett 2015;15:6261–6.
[7] Li Y, Mao H, Hu P, et al. Bioinspired functional surfaces enabled by multiscale stereolithography. Adv Mater Technol 2019;4:1800638.
[8] Fattal D, Li J, Peng Z, Fiorentino M, Beausoleil RG. Flat dielectric grating reflectors with focusing abilities. Nat Photon 2010;4:466.
[9] Yao Y, Liu H, Wu W. Spectrum splitting using multi-layer dielectric meta-surfaces for efficient solar energy harvesting. Appl Phys A 2014;115:713–9.
[10] Yao Y, Liu H, Wu W. Fabrication of high-contrast gratings for a parallel spectrum splitting dispersive element in a concentrated photovoltaic system. J Vac Sci Technol B Nanotechnol Microelectron 2014;32:06FG04.
[11] Yao Y, Liu H, Wu W. Fabrication of high contrast gratings for the spectrum splitting dispersive element in a concentrated photovoltaic system. JoVE 2015;101:e52913.
[12] Yao Y, Wu W. All-dielectric heterogeneous metasurface as an efficient ultra-broadband reflector. Adv Opt Mater 2017;5:1700090.
[13] Liu H, Yao Y, Wu W. Reflective color display based on tunable sub-wavelength high contrast gratings. U. S. Patent 9,733,402, Issued August 15, 2017.
[14] Liu H, Yao Y, Wang Y, Wu W. Full-color reflective display system based on high contrast gratings. J Vac Sci Technol B Nanotechnol Microelectron 2014;32:06FE04.
[15] Liu H, Yang H, Li Y, et al. Switchable all-dielectric metasurfaces for full-color reflective display. Adv Opt Mater 2019;7:1801639.
[16] Ha J, Ndao A, Hsu L, Park J-H, Kante B. Planar dielectric cylindrical lens at 800 nm and the role of fabrication imperfections. Opt Exp 2018;26:23178–84.
[17] Penninck L, Woestenborghs W. Quantifying fabrication errors in meta-lenses by Monte Carlo simulations. Metamater Metadev Metasyst 2019;2019:110800H.
[18] Johnson SG, Povinelli M, Soljačić M, Karalis A, Jacobs S, Joannopoulos J. Roughness losses and volume-current methods in photonic-crystal waveguides. Appl Phys B 2005;81:283–93.
[19] Bruno TJ, Svoronos PD. CRC handbook of fundamental spectroscopic correlation charts. CRC Press, 2005.
[20] Devlin RC, Khorasaninejad M, Chen WT, Oh J, Capasso F. Broadband high-efficiency dielectric metasurfaces for the visible spectrum. Proc Natl Acad Sci 2016;113:10473–8.
[21] Lukosz W, Kunz R. Light emission by magnetic and electric dipoles close to a plane interface. I. Total radiated power. J Opt Soc Am 1977;67:1607–15.
[22] Decker M, Staude I. Resonant dielectric nanostructures: a low-loss platform for functional nanophotonics. J Opt 2016;18:103001.
[23] Nordendorf G, Hoischen A, Schmidtke J, Wilkes D, Kitzerow HS. Polymer-stabilized blue phases: promising mesophases for a new generation of liquid crystal displays. Polym Adv Technol 2014;25:1195–207.
[24] Wu Y-KR, Hollowell AE, Zhang C, Guo LJ. Angle-insensitive structural colours based on metallic nanocavities and coloured pixels beyond the diffraction limit. Sci Rep 2013;3:1–6.
[25] Heikenfeld J, Drzaic P, Yeo JS, Koch T. A critical review of the present and future prospects for electronic paper. J Soc Inf Disp 2011;19:129–56.
[26] Franklin D, George M, Fraser J, Chanda D. Atomic layer deposition tuning of subwavelength aluminum grating for angle-insensitive plasmonic color. ACS Appl Nano Mater 2018;1:5210–6.
[27] Ji C, Acharya S, Yamada K, Maldonado S, Guo LJ. Electrodeposition of large area, angle-insensitive multilayered structural colors. ACS Appl Mater Interfaces 2019;11:29065–71.
[28] Safaei A, Chandra S, Leuenberger MN, Chanda D. Wide angle dynamically tunable enhanced infrared absorption on large-area nanopatterned graphene. ACS Nano 2018;13:421–8.
[29] Song B, Yao Y, Groenewald RE, et al. Probing gap plasmons down to subnanometer scales using collapsible nanofingers. ACS Nano 2017;11:5836–43.
[30] Yao Y, Liu H, Wang Y, et al. Nanoimprint lithography: an enabling technology for nanophotonics. Appl Phys A 2015;121:327–33.
[31] Li Y, Mao H, Liu H, et al. Stereolithography with variable resolutions using optical filter with high-contrast gratings. J Vac Sci Technol B Nanotechnol Microelectron 2015;33:06F604.
[32] Chou SY, Krauss PR, Renstrom PJ. Imprint lithography with 25-nanometer resolution. Science 1996;272:85–7.
[33] Yao Y, Liu H, Wang Y, et al. Nanoimprint-defined, large-area meta-surfaces for unidirectional optical transmission with superior extinction in the visible-to-infrared range. Opt Express 2016;24:15362–72.
[34] Yao Y, Wang Y, Liu H, Li Y, Song B, Wu W. Line width tuning and smoothening for periodical grating fabrication in nanoimprint lithography. Appl Phys A 2015;121:399–403.

Supplementary Material: The online version of this article offers supplementary material (https://doi.org/10.1515/nanoph-2019-0501).